1 **Multidimensional imbalances in cortical circuit activity in Fragile-X**

2 **Syndrome mice**

3 Cian O'Donnell[1,2,*], J. Tiago Gonçalves[3,4], Carlos Portera-Cailliau[3] and Terrence J.

4 Sejnowski[2,5,*]

5 [1]Department of Computer Science, University of Bristol, Bristol, UK

6 [2]Howard Hughes Medical Institute, Salk Institute for Biological Studies, La Jolla CA, USA

7 [3]Departments of Neurology and Neurobiology, David Geffen School of Medicine at UCLA, Los

8 Angeles, CA, USA

9 [4]Dominick Purpura Department of Neuroscience, Albert Einstein College of Medicine, Bronx,

10 NY, USA

11 [5]Division of Biological Sciences, University of California at San Diego, La Jolla, CA, USA

12 *Correspondence: cian.odonnell@bristol.ac.uk (C.O'D.), terry@salk.edu (T.J.S.)

13 ***Abstract***

14 A leading theory for multiple brain disorders, such as schizophrenia and autism, is that they

15 arise from developmental imbalances in excitatory and inhibitory (E/I) brain circuitry. However,

16 it is unclear whether this simple 1-dimensional model is sufficiently rich to capture the set of

17 key alterations of neural circuit processing in brain disorders. Here we used a combination of

18 computational modeling and large-scale analysis of *in vivo* 2-photon Ca^{2+} imaging data

19 from somatosensory cortex of wild-type and *Fmr1* knock-out (KO) mice, a model of Fragile X

20 syndrome, to test the E/I imbalance model. Our main findings were: 1) the E/I imbalance model

21 was not rich enough to capture the alterations in neural activity statistics in *Fmr1* KO mice; 2)

22 in a computational model we found greatly varying magnitudes and directions of effects of

23 synaptic and cellular properties on network activity; 3) evidence for opposite changes in circuit

24 properties of *Fmr1* KO mice at different stages of development; 4) a reduction in the entropy

25 of circuit activity in young *Fmr1* KO mice compared to wild-type, but an opposite increase in

26 adult *Fmr1* KO mice. These findings suggest qualitatively new strategies for developing

27 treatments for Fragile-X Syndrome and related disorders.

Introduction

The nervous system shows complex organization at many spatial scales: from genes and molecules, to cells and synapses, to neural circuits. Ultimately, the electrical and chemical signaling at all of these levels must give rise to the behavioral and cognitive processes seen at the whole-organism level. When trying to understand prevalent brain disorders such as Autism and Schizophrenia, a natural question to ask is: where does the most productive level of neuroscientific investigation lie? Traditionally, most major disorders are diagnosed entirely at the behavioral level, whereas pharmaceutical interventions are targeted at correcting alterations at the molecular level. Even for the most successful drugs, we have little understanding of how these pharmaceutical actions at the molecular level percolate up the organizational ladder to affect behavior and cognition. This implies that a promising level of analysis might be at the intermediate level of neural circuits, for two reasons. First, circuits are closer to the behavioral level than the molecular signaling of cells is; therefore, it might be easier to predict how interventions at the circuit level affect behavior. Second, since we have fewer neurons than molecules and fewer neural circuits than neurons, the dimensionality of the brain's neural circuit properties is likely much smaller than that of the brain's molecular properties. It might turn out to be easier to find interventions to push circuit-level properties of brain disorder patients towards the operating regimes observed in healthy subjects, than it would be to correct the corresponding deficits in patients at the molecular level.

One prominent circuit-level hypothesis for brain disorders has been the idea of an imbalance in excitatory and inhibitory signaling. First proposed as a model for Autism (Rubenstein and Merzenich, 2003), the concept has since been applied to many other brain disorders, including Schizophrenia, Rett Syndrome, Fragile-X Syndrome, Tuberous Sclerosis, and Angelman Syndrome (Bateup et al., 2011; Dani et al., 2005; Gibson et al., 2008; Kehrer et al., 2008; Wallace et al., 2012). However, a major drawback of this model in its simplest form is that it is entirely 1-dimensional. It implies that either too much excitation or too much inhibition is unhealthy, and by extension that the symptoms of these disorders could be normalized by either enhancing or reducing the level of, say, GABAergic signaling as appropriate. Although

56   clinical trials for such GABAergic-based interventions are ongoing (Braat and Kooy, 2015), no

57   treatment for a neurodevelopmental disorder based on this principle has yet been validated.

58   In this study we compare *in vivo* neocortical circuit activity data recorded from wild-type and

59   Fragile-X model mice, and find that the classic 1-dimensional E/I imbalance model is not

60   flexible enough to capture the observed differences. Instead, we argue that higher-dimensional

61   models are needed. We demonstrate that a novel 2D neural circuit model can account for

62   many of the differences in circuit activity that are likely important for neural coding and

63   information processing. Finally, we apply a recently developed large-scale data analysis

64   method to our Ca^{2+} imaging data to uncover systematic shifts in neural circuit entropy across

65   development in Fragile-X.

Results

Neural circuits consist of many components, connected together in a complicated fashion. These components typically interact non-linearly to generate circuit activity dynamics. Although many properties of cortical circuit components have been found to be altered in animal models of brain disorders, it remains extremely difficult to predict the net effect of varying any one particular parameter on circuit behavior.

To explore this issue more concretely, we built a computational model of layer (L) 2/3 mouse somatosensory cortex. This circuit has been studied in detail by neurophysiologists, and several of its properties have been found to be altered during development in mouse models of Fragile-X syndrome, including parvalbumin-positive interneuron number (Selby et al., 2007), GABA receptor reversal potential (He et al., 2014), dendritic spine dynamics (Cruz-Martin et al., 2010), and L4 excitatory input (Bureau et al., 2008), reviewed by (Contractor et al., 2015). In the ideal case we would like to derive a mathematical relationship between any arbitrary circuit parameter and its effect on circuit function, but for even reasonably complicated models this problem quickly becomes analytically intractable. Because of this difficulty, we used numerical computer simulations to perform hypothetical experiments where we perturbed various parameters of the circuit model and observed the resulting changes in circuit-level activity dynamics.

The L2/3 computational model we built (Figure 1A, see Methods for details) consisted of four interconnected populations of leaky integrate-and-fire neurons: one group of 1700 excitatory (E) pyramidal neurons and three groups of inhibitory neurons: 115 $5HT_{3A}$R-expressing neurons, 70 parvalbumin-expressing (PV) neurons, and 45 somatostatin-expressing (SOM) neurons. This L2/3 circuit was driven by a separate population of 1500 L4 excitatory neurons. Cellular numbers, intrinsic properties, synaptic strengths, and connectivity statistics were taken from published *in vitro* data from P17—22 wild-type mice (Avermann et al., 2012; Lefort et al., 2009; Tomm et al., 2014).

L2/3 neurons of the rodent somatosensory neocortex respond only sparsely to sensory stimulation *in vivo*. For example, twitching a whisker activates only ~20% of neurons on

94   average, each of which typically emits only one action potential (Clancy et al., 2015; Kerr et al.,

95   2007; Sato et al., 2007). Hence any individual neuron carries very little information about the

96   stimulus on its own, implying that information must instead be encoded at the circuit level as

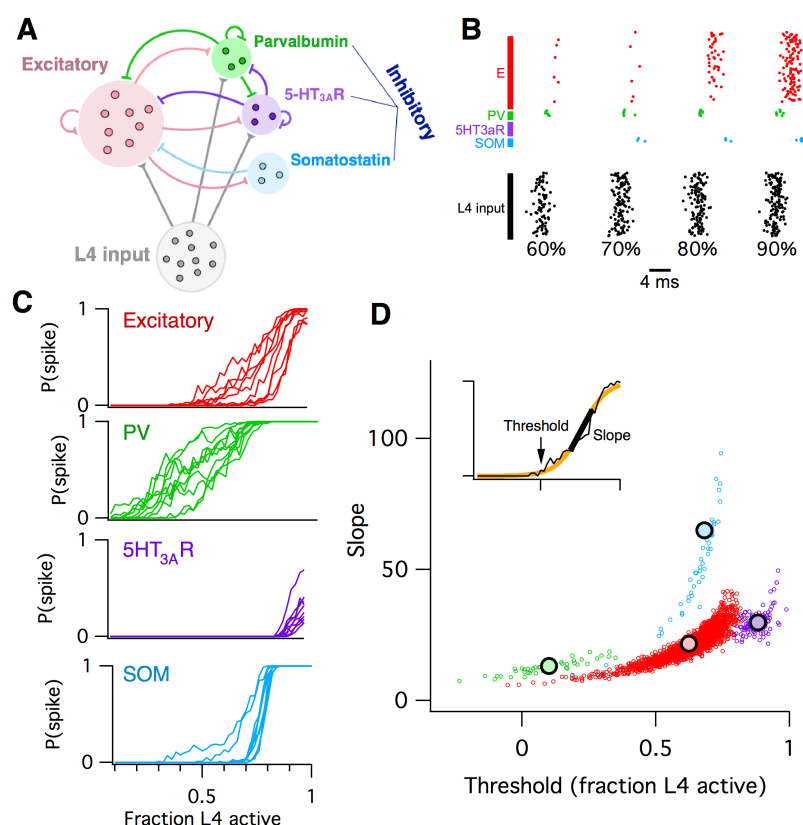97   the identities of the subset of neurons that respond.

Figure 1. Computational model of L2/3 mouse somatosensory cortex.
A: Schematic diagram of computational circuit model.
B: Example raster plots of spiking responses from a subset of neurons from each cell type (colors as in panel A), for varying fractions of L4 activated (black).
C: Probability of spiking as a function of the fraction of L4 neurons activated. Each curve represents the response probability of a single neuron, averaged over multiple trials and multiple permutations of active L4 cells.
D: Each circle plots the fitted logistic slope and threshold values for a single neuron in the simulation. Circle color indicates cell type: red is excitatory, green is PV inhibitory, purple is 5ht3AR inhibitory, blue is SOM inhibitory. Inset shows an example fitted logistic response function (orange) to the noisy simulation results from a single excitatory neuron (black).

98   To model whisker twitching, we simulated a volley of spikes arriving from L4 as input to the

99   population of L2/3 cells. We chose a random subset of L4 neurons as ON, then sent a single

100   spike from each of these L4 cells to their target neurons in L2/3, and recorded the responses of

101 all neurons in L2/3, some of which spiked and some of which did not. We repeated this

102 identical stimulation multiple times, in order to get an average response probability for each

103 L2/3 neuron, given the probabilistic vesicle release at synapses in the model. Then we chose a

104 different random subset of L4 neurons as ON, and repeated the entire procedure. Finally, we

105 varied the fraction of L4 cells active and plotted the probability of response for each individual

106 L2/3 neuron as a function of L4 activity level (Figure 1B—C).

107 We found that the mean response probability of each neuron in the simulation increased from

108 zero to one monotonically with increasing L4 activity level. However, the shape of the response

109 curve varied systematically across cell types, and was heterogeneous for different neurons of a

110 given cell type. To quantify these differences, we used logistic regression to fit the response

111 profile of each neuron with a sigmoid function (Figure 1D, inset), which has just two

112 parameters: the slope (representing the steepness of the response curve) and threshold

113 (representing the minimal fraction of L4 neurons needed to activate the cell). When we plotted

114 the fitted slope and threshold values for each neuron against each other, we found that each

115 cell type falls into a distinct cluster in this 2-dimensional space. For example, all PV inhibitory

116 neurons had a low slope and low threshold, whereas SOM inhibitory neurons had a steep

117 slope and moderate threshold. We will use these slope-threshold measurements to summarize

118 the circuit-level input-output function of this 'default' model of L2/3 somatosensory cortex.

119 The circuit model contains 100 parameters (Methods), several of which are altered in Fragile-X

120 mouse models. How sensitive is the circuit's macroscopic input-output function to alterations in

121 its low-level components? To test this, we varied 76 of the model parameters in turn by ±20%,

122 and repeated the entire set of simulations for each case (Methods). For each individual

123 parameter alteration, we fit a new logistic response function for each model neuron. We

124 summarize the results by plotting the logistic slope and threshold parameters and comparing

125 their values to those found with the default model. The outcomes were hugely varied. We show

126 three examples from the set of fifty-nine in Figure 2A. First, when we increased the amplitude

127 of postsynaptic potentials (PSPs) of excitatory synapses from L4 to L2/3 excitatory neurons,

128 we found that the logistic threshold parameter of all cell types shifted leftwards to lower values

129 (Figure 2A left), implying that fewer L4 neurons were needed to activate the entire L2/3 circuit.

130   In contrast, when we increased the PSP amplitude of a different excitatory synapse, the

131   recurrent connections between L2/3 excitatory neurons, we found (Figure 2A center) that

132   excitatory and SOM inhibitory neurons had increased slope parameters relative to default, with

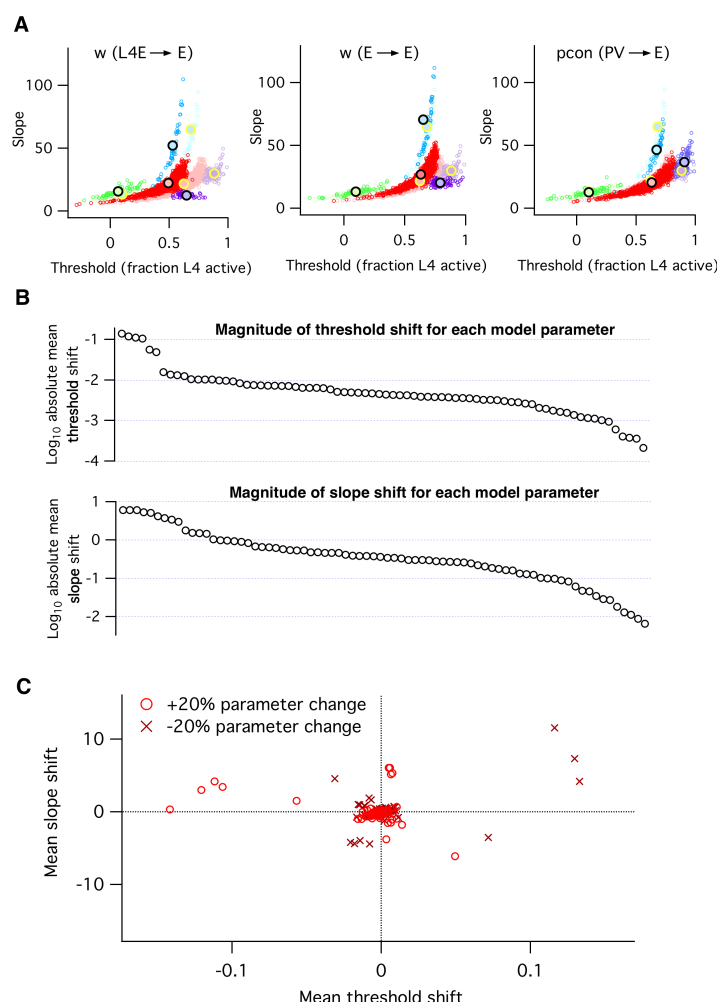133   little change in their threshold parameters. 5HT$_{3A}$R

Figure 2. Heterogeneous effects of varying L2/3 parameters on the circuit input-output function.
A: Shifts in the distribution of fitted slope and threshold parameters as a result of increasing the strength of synapses from L4 to L2/3 E neurons (left), increasing the strength of recurrent synapses between L2/3 E neurons (center), or increasing the connection probability between L2/3 PV interneurons and E neurons (right). Transparent circles represent values for default network, heavy circles for altered network. The default and altered group means are large yellow and black open circles, respectively.
B: Absolute values of mean shifts in threshold (upper plot) and slope (lower plot) for E neurons arising from increasing the value of each parameter by +20%. Note that data are presented on a log10 scale.
C: The shift in mean slope-threshold parameter values for E neurons from the default

> network values, in response to each of the 59 circuit parameter alterations. Light red circles indicate +20% increase in parameter value; dark red crosses indicate a -20% decrease in parameter value.

134   inhibitory neurons had decreased slopes and thresholds, while PV neurons had little change at

135   all. As a third example we increased the probability of inhibitory synaptic connections from L2/3

136   PV interneurons to L2/3 excitatory neurons (Figure 2A right). In this case we found that

137   excitatory neurons had a lower slope and increased threshold, SOM inhibitory neurons had a

138   lower slope, $5HT_{3A}R$ inhibitory neurons had both an increased slope and threshold, and PV

139   neurons showed little change, even though their outgoing synapses were the parameter that

140   was altered.

141   To synthesize the findings from all simulations, for each altered parameter we plot the shift in

142   mean slope-threshold values for L2/3 excitatory neurons from the mean values found with the

143   default model (Figure 2B). We focus on excitatory neurons because they constitute 90% of the

144   neurons in this layer (Lefort et al., 2009) and are the primary output to downstream circuits

145   (Mao et al., 2011; Petreanu et al., 2007). Overall, we found a very heterogeneous picture. First,

146   the magnitude of the shift in circuit response varied dramatically from parameter to parameter

147   (Figure 2B—C). Varying some parameters, such as the first two examples given above, had

148   large effects, whereas varying other parameters such as w_{l5htE} (the strength of synapses from

149   $5HT_{3A}R$ inhibitory neurons to E neurons) or τm_{lsom} (the membrane time constant of SOM

150   inhibitory neurons) had little effect. Second, the direction of shift in 2-D slope-threshold space

151   also depended on parameter (Figure 2C). Increasing some parameters changed either circuit

152   slope or threshold in isolation, while other parameters changed both slope and threshold

153   together. All four quadrants of the slope-threshold plane could be reached by various subsets

154   of the model parameters. Third, basic knowledge of whether a component was 'excitatory' or

155   'inhibitory' was insufficient to predict the direction of slope-threshold change. For example, the

156   two glutamatergic projections considered in Figure 2A had distinct effects on circuit function.

157   In summary, these simulations indicate that the L2/3 somatosensory cortex circuit has

158   extremely varied sensitivities to changes in its cellular components, and that the eventual

159   circuit-level consequences cannot be predicted from knowledge of the class of the perturbed

160   neurotransmitter alone.

Firing rates and correlations from the logistic model

161

162 Above we investigated how low-level circuit components affect a high-level circuit input-output

163 function, as parameterized by the slope and threshold of fitted logistic functions. But how is this

164 logistic input-output function related to more common measures of neural population activity,

165 such as firing rates and pairwise correlations between neurons? To investigate this, we

166 considered the following reduced statistical model of cortical activity. We assumed for

167 simplicity that the magnitude of the total input to the L2/3 circuit is a Gaussian distributed

168 random variable, with zero mean and unit standard deviation (Figure 3A lower left). Then we

169 described each L2/3 neuron's input-output as a logistic function as before (Figure 3A upper

170 left), with threshold and slope defined relative to the Gaussian input's mean and standard

171 deviation, respectively. Given this model, we can numerically calculate the probability

172 distribution over a neuron's firing probability, which in general is skewed and non-Gaussian

173 (Figure 3A upper right). From this function we compute (Methods) both the neuron's mean

174 firing probability and the pairwise correlation of two identical neurons following this profile

175 (Figure 3A lower right).

176 Neural firing rates and correlations had qualitatively different dependencies on the underlying

177 logistic model's slope and threshold. Neural firing rate was greatest when threshold was low

178 and slope was high (top left of phase plot, Figure 3C left), whereas correlations were greatest

179 when both threshold and slope were high (top right of phase plot, Figure 3C right). This implies

180 that any change in the circuit's input-output function slope or threshold will in general have

181 distinct effects on firing rate versus correlations, and so could not be captured by a 1-

182 dimensional E/I balance model that sought to normalize firing rates alone. To illustrate this fact,

183 we plot the calculated correlation values along a contour where firing probability is fixed at 0.1

184 (Figure 3D). In the region of parameter space where both the slope and threshold are low

185 (Figure 3C bottom left), correlations are low, ~0.01. However, as we move along the contour

186 for firing rate = 0.1 towards the region of parameter space where slope and threshold are high

187 (Figure 3C top right), the pairwise correlations increase to ~0.4. This shows that a 1-

188 dimensional E/I balance rule that exclusively sought to normalize neural firing rates would

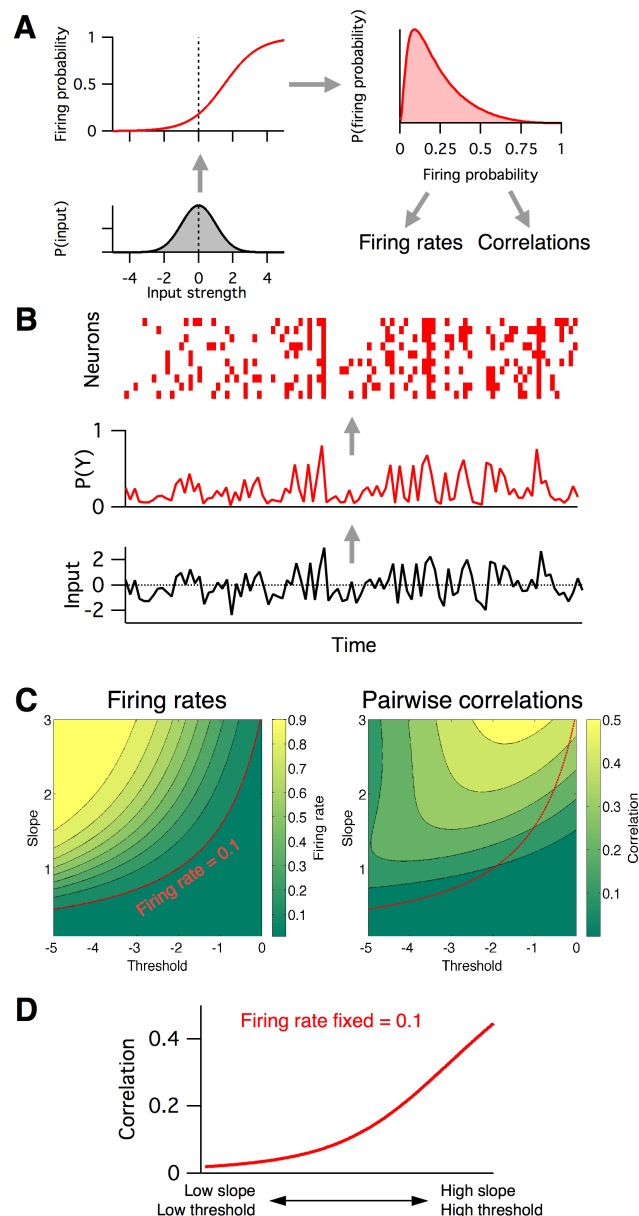189 leave neural correlations free to achieve arbitrary values.

Figure 3. Firing rates and pairwise correlations from the logistic response model.
A: Logistic model components. We assume a normally distributed input drive (gray distribution, bottom left), which is passed through the neuron's probabilistic spike input-output function (red curve, top left), which results in a distribution of spike probabilities (top right) that are determined by the input-output function's slope and threshold parameters. From the output distribution we can directly calculate the mean firing rate and correlation between a pair of such neurons (Methods).
B: Example spikes from the logistic model. The bottom trace (black) shows examples inputs over time drawn randomly from the same normal distribution. This is transformed to spike probability at each time point (red trace). Example spike trains can then be generated from the spike probability trace by drawing Bernoulli samples with the specified probabilities (red ticks, top). If each neuron's spike train is conditionally independent given the same spike

10

probabilities, we can see correlations in their spike trains.

C: Calculated mean firing rate (left) and pairwise correlation (right) color maps as a function of the logistic threshold (x-axis) and slope (y-axis) parameters. Contours indicate lines of fixed firing rate or correlation in the 2D slope-threshold space.

D: Pairwise correlation values along the slope-threshold contour for firing rate = 0.1.

190

191 How might these findings inform our understanding of neurodevelopmental disorders, such as

192 Fragile-X syndrome? To explore this we fit the parameters of the logistic model to reproduce

193 the statistics of spontaneous activity recorded from populations of neurons in unanesthetized

194 mouse somatosensory cortex using in vivo two-photon Ca^{2+} imaging (data previously

195 published in (Gonçalves et al., 2013), see Methods for experimental details). We compared the

196 data from wild-type (WT) mice with *Frm1* KO mice, the best studied animal model for Fragile-X

197 syndrome, across three different developmental time points: just before (P9—11) and after

198 (P14—16) the critical period, and a more mature timepoint (P30—40). Example ΔF/F raster

199 plots from each group are shown in Figure 4A. We binned the data into 1 s timebins (originally

200 imaged at 4 Hz), then transformed each neuron's timeseries of ΔF/F values into a probabilistic

201 sequence of binary ON/OFF values by assuming a Poisson firing model (Methods). We then

202 summarized the neural population activity from each animal with three statistics: the mean ON

203 probability across all recorded neurons (Figure 4C), the standard deviation (s.d.) in ON

204 probability across neurons (Figure 4D), and the mean correlation between all pairs of neurons

205 (Figure 4E). Together these measures capture both the statistics of the bulk population activity

206 and some indication of the heterogeneity across neurons. For mean firing rates, the only

207 change we detected was a decrease in firing probability in WT between P14—16 and P30—40

208 (p = 0.027), which was coupled with an increased s.d. of firing rates (p = 0.015). We also

209 detected a higher firing rate s.d. in P9—11 KO animals than WT (p = 0.031). Finally, as

210 previously reported (Golshani et al., 2009; Gonçalves et al., 2013; Rochefort et al., 2009), we

211 found a substantial decrease in pairwise correlations in both genotypes across development,

212 with slightly higher correlations in KO animals than WT at P9—11 (p = 0.029) and P14—16 (p

213 = 0.047). These results are consistent with a general model where neural firing becomes

214 desynchronized and sparsified around the critical period, at least in WT animals (Golshani et

215 al., 2009; Rochefort et al., 2009).

11

216   For the three summary statistics from each animal, we used a gradient descent algorithm to

217   find the five parameters of a population-level version of the logistic model that best matched

218   the activity statistics (see Methods). For each animal, we plot the mean slope and mean

219   threshold fits (Figure 4F) on top of the previously calculated (Figure 3C) 2D slope-threshold

220   maps of firing rate and correlation. We find that in young animals, P9—11, most points are

221   scattered at high values of both slope and threshold (Figure 4D left). With age, the parameter

222   fits for both genotypes moved south-west towards the low slope and low threshold region of

223   parameter space (Figure 4D center and right). The mean location of the cloud of points at each

224   developmental age differed between WT and KO. We plot the direction of shift in group mean

225   from WT to KO in Figure 4G. In young animals, P9—11 and P14—16, the KO group had both

226   higher slope and higher threshold than WT, whereas in adult animals, P30—40, the KO group

227   had a lower slope and lower threshold than WT. These results demonstrate an opposite

228   direction of circuit parameter change in young Fragile-X mice compared to adults, which could

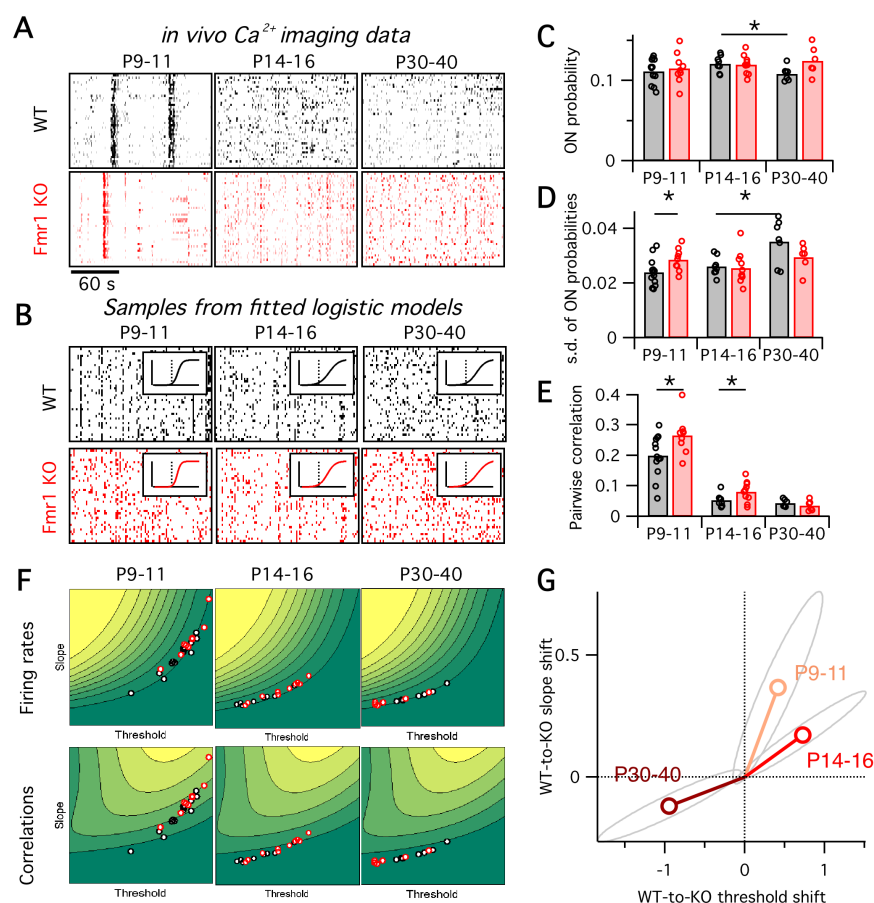229   not be captured by examining either neural firing rates or correlations.

12

Figure 4. Fragile-X fits from logistic model.

A: Example Ca^{2+} imaging dF/F raster plots from a single animal from each of two genotypes, WT and *Frm1* KO, and three age groups, P9—11, P14—16 and P30—40. In each case 3 minutes of data are shown from 40 neurons.

B: Example samples from the fitted logistic models, corresponding to the six groups shown in panel A. Inset shows group mean fitted logistic function, dashed vertical line represents zero.

C-E: Mean firing probability (C), standard deviation of firing probabilities (D) and mean pairwise correlation across all neurons (E). Each circle represents data from a single animal, bars represent group means.

F: Fitted logistic mean slope and mean threshold values for data from each WT (black circles) and *Fmr1* KO (red circles) animal. Values overlaid on same firing rate (top) and correlation (bottom) maps from Figure 3C.

G: Shift in mean logistic slope and threshold values from WT to KO for P9—11 (orange), P14—16 (red) and P30—40 (brown). Grey ellipses represent 95% confidence intervals (Methods).

230

231   Earlier we asked how sensitive the logistic model slope and threshold parameters were to

232   alterations in the many underlying neural circuit components (Figure 2). In a similar way, we

233 can also ask how sensitive the neural firing rates and correlations are to alterations in the

234 logistic slope and threshold parameters. This is important since inspection of the 2-dimensional

235 maps in Figure 2C shows that these sensitivities will differ depending on starting location within

236 the slope-threshold space. To quantify this effect, we calculated the sensitivity of both the firing

237 rate and correlations to small changes in the slope and threshold (Figure 5, see Methods),

238 local to the fitted logistic parameter values for each animal (black and red circles in Figure 4F).

239 Across all animals, we found that changes in the slope and threshold were qualitatively

240 consistent but quantitatively inconsistent. Increasing the slope or decreasing the threshold

241 always increased both firing rates and correlations. However, the magnitude of these effects

242 depended strongly on developmental age (we found only minor differences between genotypes

243 at any age). In young animals, P9—11, changes in the logistic threshold (solid bars in Figure

244 5) had substantial effects on both firing rates and correlation. This sensitivity decreased with

245 age ($p \leq 0.013$ for firing rates, $p < 0.01$ for correlations from P9—11 to P14—16, both for

246 pooled data across genotypes), so that in adult animals, P30-40, changes in threshold had

247 relatively little effect on neural activity statistics. A different picture emerged for the logistic

248 slope parameter (striped bars in Figure 5). There, the firing rate sensitivity increased with from

249 P9—11 to P14—16 ($p < 1e-6$) (Figure 5A), while correlation sensitivity stayed approximately

250 constant ($p \geq 0.18$) (Figure 5B). These results show that the quantitative relationships between

251 neural activity statistics and the underlying circuit parameters are not fixed across development.
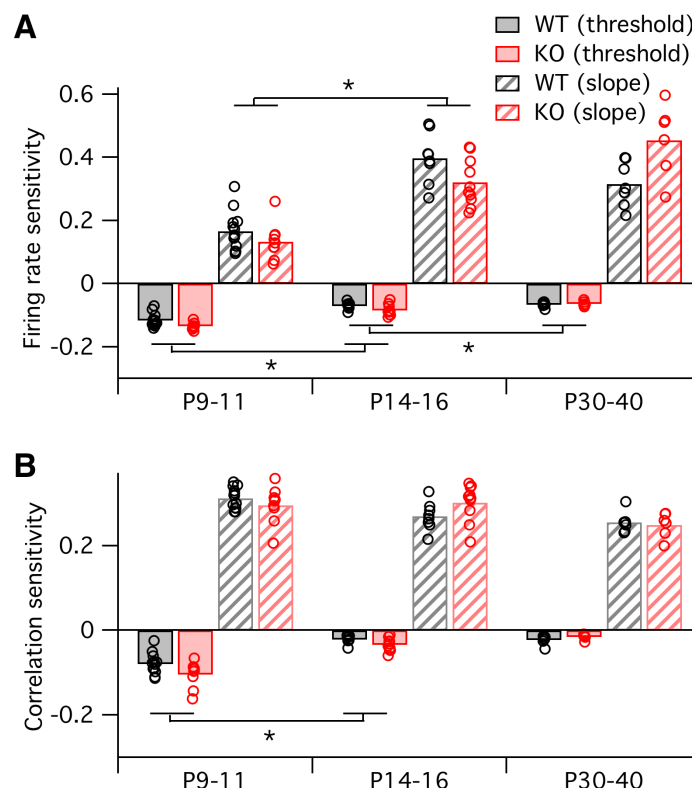
Figure 5. Sensitivity of firing rate and correlations with respect to logistic model parameters, local to the parameter fit for each animal.
Sensitivity of firing probability (**A**) and pairwise correlations (**B**) to change in threshold (solid bars) and slope (striped bars) parameters of logistic model, about the fitted parameter values for each animal (circles) displayed in Figure 4F. Bars represent group means.

252

253   What are the functional implications of these alterations in firing rates and correlations in

254   Fragile-X mice across development? To address this, we attempted to calculate the entropy of

255   the neural population activity for the data from each animal. Entropy is a quantity from

256   information theory, measured in bits, that puts a hard upper bound on the amount of

257   information that can be represented by any coding system (Cover and Thomas, 2006).

258   Intuitively, the entropy measures how uniform the neural population activity pattern distribution

259   is: it is large if the circuit exhibits many different activity patterns over time, and small if only a

260   few activity patterns dominate. Entropy is an appealing measure for the present problem

261   because it is sensitive both to neural firing rates and to correlations at all orders. It is typically

262   highest when firing rates are high and correlations are low. Although entropy is notoriously

15

263 difficult to calculate for large neural populations because most estimation methods require

264 impractically long data recordings (Quian Quiroga and Panzeri, 2009), we recently developed a

265 new statistical method for this purpose, called the *population tracking model*, that scales well to

266 large numbers of neurons, even for limited data (O'Donnell et al., in press). We fit this

267 population tracking model to the same Ca^{2+} imaging data as analyzed above (Figure 6). An

268 intermediate step in estimating the neural entropy involves calculating a low-parameter

269 approximation of the entire probability distribution over all 2^N neural population activity patterns,

270 where N is the number of neurons. The cumulatives of these probability distributions calculated

271 for 50-neuron subsets of the recordings are shown in Figure 6A. In young animals P9—11, a

272 small number of activity patterns accounts for a large fraction of the probability mass (Figure

273 6A left). For example, based on these curves, 50% of the time we would expect to see the

274 same 1000—10,000 patterns out of a possible total $2^{50} \approx 10^{15}$ patterns. In contrast, in older

275 animals P14—16 and P30—40 the cumulative distributions shift rightwards so that more

276 patterns are typically observed (Figure 6A center, right). In these cases, around 1,000,000

277 patterns are needed to account for 50% probability mass.

278 Instead of attempting to quantify these shifts by asking how many patterns are needed to cross

279 an arbitrary threshold of probability mass, we instead calculated the entropy, which takes into

280 account the shape of the entire probability distribution. The entropy depends the number of

281 neurons analyzed, so we normalized all estimates to calculate the entropy per neuron (Figure

282 6B—C). Since we are treating neurons as binary, the entropy/neuron was bounded between 0

283 and 1 bits. For all age groups, and for both WT and *Fmr1* KO animals, entropy/neuron

284 progressively decreased with the number of neurons analyzed (Figure 6B). Because each

285 imaging session captured a different number of neurons (range 40—198, median 97), we fit

286 the entropy/neuron versus number of neurons data with a double exponential function (see

287 Methods) and use the fit to provide a standardized estimate of the entropy/neuron for 100-

288 neuron populations (Figure 6C). In WT animals, entropy/neuron showed a non-monotonic

289 trajectory across development (O'Donnell et al., in press). At P9—11 it was low, 0.38 bits (95%

290 c.i. [0.35:0.41]), before increasing at P14—16 (p < 0.001) to 0.50 bits (95% c.i. [0.48:0.52]),

291 before decreasing again at P30—40 (p = 0.028) to 0.45 bits (95% c.i. [0.42:0.48]). We found a

292 different entropy trajectory in *Frm1* KO animals. There, although entropy/neuron also began
293 low at 0.34 bits (95% c.i. [0.30:0.39]), not different from WT (p= 0.19), when it increased at
294 P14—16 (p < 0.001) to 0.465 bits (95% c.i. [0.45:0.48]) it remained lower than for WT (p =
295 0.048). Finally, instead of decreasing as in the WT case, entropy continued to increase in
296 P30—40 *Fmr1* KO animals (p = 0.033) to 0.51 bits (95% c.i. [0.47:0.55]), higher than WT (p =
297 0.034). These entropy values estimated directly from Ca^{2+} imaging data agreed well with
298 entropy estimates for synthetic data sampled from the previously fit logistic models
299 (Supplementary Figure 1). In summary, unlike WT animals, *Fmr1* KO mice showed a
300 monotonically increasing entropy/neuron from P9—11 to P30—40. Furthermore, the direction
301 of change in entropy between P14—16 and P30—40 was opposite for WT and *Fmr1* KO
302 animals, decreasing in the former and increasing in the latter.
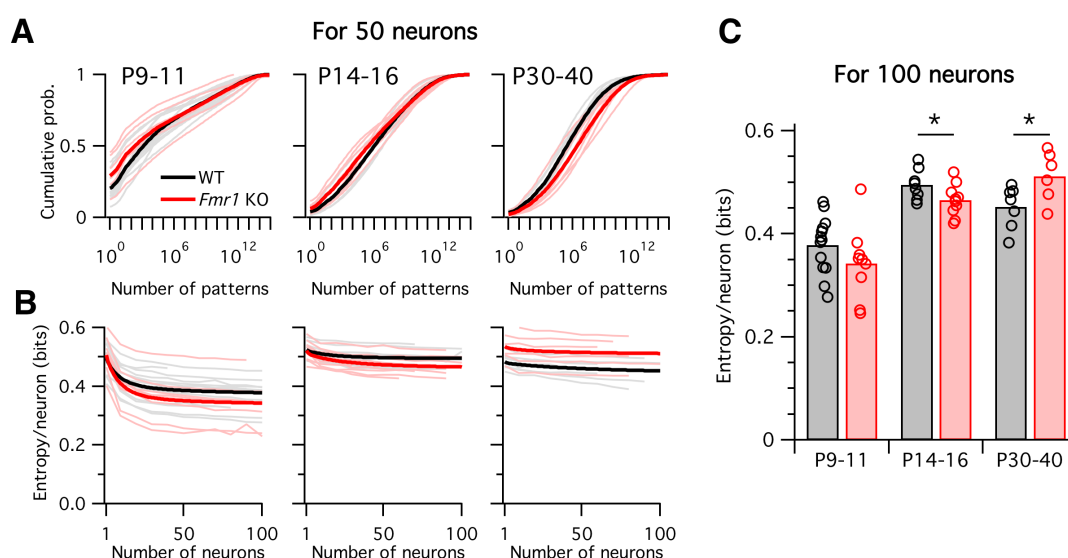
Figure 6. Differing trajectories of WT and KO entropy across development.
A: Cumulative probability mass as a function of the number of patterns. Patterns ordered from most probable to least probable. Thin lines are mean across many randomly-chosen 50-neuron subsets from a given animal, and thick lines represent means across all animals of a given genotype.
B: Entropy per neuron as a function of the number of neurons analyzed. Thin lines are mean across many randomly chosen subsets for a given animal, thick lines are group mean of double exponential fits to the data (see Methods). Age groups (left to right) are as in panel A.
C: Estimated entropy/neuron for 100 neuron populations. Circles represent individual animals, bars are group means.

303

Discussion

304

305 The 1-dimensional E/I imbalance model has been widely used for interpreting neural circuit

306 changes observed in animal models of diverse brain disorders (Bateup et al., 2011; Dani et al.,

307 2005; Gibson et al., 2008; Kehrer et al., 2008; Wallace et al., 2012). In the case of Fragile-X

308 syndrome, the hyperexcitability prediction of the E/I imbalance model is consistent with many

309 of the symptoms of the disease (e.g. seizures, hyperarousal, hyperactivity, hypersensitivity to

310 sensory stimuli) and the known pathogenic defects implicated in *Fmr1* KO mice (diminished

311 GABA signaling, exaggerated intrinsic excitability, increased neuronal firing rates; reviewed by

312 Contractor et al., 2015). Here we combined computational modeling with analysis of *in vivo*

313 neural activity data to ask whether the E/I model could also quantitatively account for

314 alterations in multiple neural activity statistics. We found that this model is too simple to

315 account for the joint alterations in neural firing rates and correlations observed in Fragile-X

316 model mice. This suggests that future studies of brain disorders may need to consider higher-

317 dimensional models of neural circuit dysfunction.

318 First, we built a detailed computational model of a specific neural circuit, L2/3 of mouse

319 somatosensory cortex (Figure 1), and asked how sensitive the spiking responses of the overall

320 circuit were to changes in its underlying neural components, many of which are known to be

321 altered in *Fmr1* KO mice (Bureau et al., 2008; Gibson et al., 2008; Gonçalves et al., 2013;

322 Harlow et al., 2010; Hays et al., 2011; Paluszkiewicz et al., 2011; Patel et al., 2013; Testa-Silva

323 et al., 2012). We found that while changing some neural parameters did have a large effect,

324 changing of other parameters had little or no effect on circuit function (Figure 2B). This

325 property, termed sloppiness, has been reported as widely prevalent in computational models of

326 biological systems (Gutenkunst et al., 2007; O'Leary et al., 2015). Its existence has two

327 important implications for studies of brain disorders: first, many of the physiological component

328 changes discovered in animal models may be entirely benign at the circuit level. Second, any

329 treatment designed to correct circuit function does not necessarily need to correct all of the

330 low-level properties in order to be successful.

331 In addition to the varying magnitudes of circuit components' effect on circuit function, we also

332 found that different components shifted the circuit input-output function in different directions,

18

333 as defined by our 2D logistic response model (Figures 1 and 2). Even circuit parameters that
334 are nominally of the same type, such as the strength of glutamatergic synapses between
335 excitatory (E) neurons in L4 to E neurons in L2/3 or synaptic strength between E neurons
336 within L2/3, had qualitatively different effects on the circuit response to stimulation (Figure 2).
337 According to the standard E/I imbalance model (Rubenstein and Merzenich, 2003), both of
338 these parameters should have similar effects on circuit function; but according to the logistic
339 response model we studied, their differing effects on slope and threshold parameters must
340 necessarily lead to different magnitudes of change in neural firing rates and correlations
341 (Figure 3C). Indeed, no 1-dimensional model of circuit function could ever capture the
342 heterogeneity in parameter sensitivities that we observed (Figure 2B).

343 Next, we fit the parameters of the logistic response model to match the *in vivo* firing statistics of
344 neural populations from WT and *Fmr1* KO mice of varying age (Figure 4). Previous studies had
345 found that neural correlations decrease during development (Golshani et al., 2009; Rochefort
346 et al., 2009), and that *Fmr1* KO mice had higher correlations and firing rates than WT mice at
347 P14–16 (Gonçalves et al., 2013; La Fata et al., 2014). A recent study suggests circuit
348 hypersynchrony is also found in different mouse models of Rett syndrome (Lu et al., 2016).
349 However, the relationship between these changes in firing statistics and the underlying neural
350 circuit components were unclear. Our logistic model helps bridge this gap, leading to two
351 findings: first, the direction of circuit parameter change from young (P9—11 and P14—16) to
352 mature (P30—40) animals is opposite in WT to KO mice (Figure 4G). Similar opposing
353 switches in sensory cortex properties with age were also recently reported in *Frm1* KO rats
354 (Berzhanskaya et al., 2016). Second, we found that the sensitivity of neural firing rates and
355 correlations to changes in underlying circuit components depends on developmental age
356 (Figure 5). Taken together, these findings imply that qualitatively different interventions may be
357 needed at different stages of development in Fragile-X, and perhaps other
358 neurodevelopmental disorders, to shift cortical circuit function towards typical wild-type
359 operation.

360 Spontaneous, intrinsic activity is ubiquitously present in mammalian cerebral cortex. It is highly
361 structured at multiple spatiotemporal scales (Mitra et al., 2015; Ringach, 2009) and interacts

362   strongly with the signals evoked by sensory stimulation (Ringach, 2009). Cellular-resolution
363   recordings in animals have shown that the patterns of spontaneous activity in neural
364   populations are representative of the ensemble of activity patterns used by the brain to
365   represent sensory stimuli (Berkes et al., 2011; Luczak et al., 2009; Miller et al., 2014). Here we
366   found that the entropy of spontaneous activity in WT mouse somatosensory cortex follows an
367   inverted-U shaped trajectory across development, and that this trajectory is dramatically
368   altered in the *Fmr1* KO mouse model of Fragile-X (Figure 6). Although we saw no reliable
369   differences across genotypes in early postnatal animals (P9—11), *Fmr1* KO animals showed
370   lower entropy than WT after the second postnatal week (P14—16), while surprisingly switching
371   to show higher entropy than WT in adult (P30—40). Notably, this switch in the direction of
372   entropy change from WT to KO during development mirrors the reversing we saw in logistic
373   model parameter changes in Figure 4G. Together, these findings suggest a perturbed
374   trajectory of cortical development during the critical period in *Fmr1* KO mice (Meredith et al.,
375   2012). However, our results cannot distinguish whether the observed perturbation in L2/3
376   activity statistics reflects a developmental delay, or a permanently altered developmental
377   trajectory. Further studies at later developmental time points are needed.

378   What is the functional significance of these shifts in population entropy? Previous work
379   suggested that the entropy of neural circuit activity may be optimally tuned at intermediate
380   levels as a trade-off between maximizing representational capacity at high entropy, versus
381   maintaining error correction and regularization at low entropy (Schneidman et al., 2006). These
382   properties can also be thought of as trading off between discrimination and generalization,
383   respectively (Qian and Lipkin, 2011). If we assume that WT mice are optimally tuned, our
384   findings predict that young *Fmr1* KO mice should show poorer somatosensory discrimination in
385   behavioral tasks than wild-type animals, while in contrast adult *Fmr1* KO mice should perform
386   more poorly on tasks involving generalization across somatosensory stimuli.

387   If the 1-dimensional E/I imbalance model is not sufficiently rich to capture the circuit changes
388   observed in neurodevelopmental disorders, what should it be replaced with? How many
389   dimensions or degrees of freedom should a working model for a brain disorder have? We
390   suggest that the most promising approach is to start by considering the computational function

391 of a particular neural circuit, then working backwards to design a model that is both
392 sophisticated enough to capture the key information processing features of the circuit, but
393 simple enough to interpret and link to physiological data. In this study we considered a 2-
394 parameter model of L2/3 somatosensory cortex's input-output function, which could account for
395 both neural firing rates and correlations. Other brain circuits may demand models with more
396 degrees of freedom. Crucially, the most informative models need not be those that include the
397 highest level of physiological detail. All models are ultimately wrong in the sense that they
398 make abstractions about their underlying parts, and detailed models carry the additional
399 burden of fitting many parameters, which may be difficult to adequately constrain (O'Leary et
400 al., 2015).

401 One potential use of simple parametric circuit models such as the ones we employed here may
402 be as a tool for rationally designing candidate intervention compounds and then screening their
403 effects on neural population activity. This approach could complement the traditional strategy
404 of designing drugs based on reversing molecular deficits and then assessing the drug's impact
405 on animal model behavior. Indeed, our results suggest that given the multi-dimensionality of
406 circuit properties, it may prove difficult or impossible to find a single compound that can
407 correctly reverse deficits at any age. This scenario might require a combination of drugs
408 chosen to push circuit-level properties towards the 'correct' region of parameter space. The
409 framework we have introduced in this study can facilitate this type of high-dimensional
410 intervention analysis for diverse neurodevelopmental disorders.

411

Methods

Mouse in vivo calcium imaging recording

414 All Ca^{2+} imaging data were published previously (Gonçalves et al., 2013). Briefly, data were
415 collected from male and female C57Bl/6 wild-type mice at P9–40. Mice were anesthetized with
416 isoflurane, and a cranial window was fitted over primary somatosensory cortex by stereotaxic
417 coordinates. Mice were then transferred to a two-photon microscope and headfixed to the
418 stage while still under isoflurane anesthesia. 2—4 injections of the Ca^{2+} sensitive Oregon-

419   Green BAPTA-1 (OGB) dye and sulforhodamine-101 (to visualize astrocytes) were injected

420   200 um below the dura. Calcium imaging was performed using a Ti-Sapphire Chameleon Ultra

421   II laser (Coherent) tuned to 800 nm. Imaging in unanesthetized mice began within 30-60 mins

422   of stopping the flow of isoflurane after the last OGB injection. Images were acquired using

423   ScanImage software (Pologruto et al., 2004) written in MATLAB (MathWorks). Whole-field

424   images were collected using a 20× 0.95 NA objective (Olympus) at an acquisition speed of 3.9

425   Hz (512 × 128 pixels). Several 3-minute movies were concatenated and brief segments of

426   motion artifacts were removed (always <10 s total). Data were corrected for x—y drift. Cell

427   contours were automatically detected and the average ΔF/F signal of each cell body was

428   calculated at each time point. Each ΔF/F trace was low-pass filtered using a Butterworth filter

429   (coefficient of 0.16) and deconvolved with a 2 s single-exponential kernel (Yaksi and Friedrich,

430   2006). To remove baseline noise, the standard deviation of all points below zero in each

431   deconvolved trace was calculated, multiplied by two, and set as the positive threshold level

432   below which all points in the deconvolved trace were set to zero. Estimated firing rates of the

433   neurons, r_i(t), were then obtained by multiplying the deconvolved trace by a factor previously

434   derived empirically from cell-attached recordings in vivo (Golshani et al., 2009).

435   **Computational methods**

436   Data analysis and logistic model calculations were done using MATLAB (Mathworks).

437   **Detailed layer 2/3 model simulations**

438   Layer 2/3 model simulations (Figures 1 and 2) were implemented with the Python-based

439   simulator Brian (http://briansimulator.org/) (Goodman and Brette, 2009), and results analyzed

440   with MATLAB (Mathworks). The model consisted of four populations of reciprocally connected

441   leaky integrate-and-fire neurons representing a L2/3 somatosensory barrel circuit: 1700

442   excitatory neurons, 70 PV inhibitory neurons, 115 $5HT_{3A}R$ inhibitory neurons, and 45 SOM

443   inhibitory neurons, driven by a separate population of 1500 excitatory spike sources

444   representing input from L4. Cell numbers were estimated by combining layer-specific excitatory

445   and inhibitory cell count information from Lefort et al. (2009) with the approximate percentages

446   of the three inhibitory cell groups given by Petersen and Crochet (2013). All synaptic

447   connections were formed probabilistically by drawing independent random Bernoulli variables

448   with connection type-specific probabilities. Synaptic PSP amplitudes were drawn

449   independently for each synapse from a log-normal distribution constrained by the

450   experimentally reported mean and median values for each particular connection type.

451   Synapses in the model were conductance-based, but since synaptic strengths reported in the

452   literature were typically in terms of EPSP/IPSP amplitude, in accordance with how the

453   experiments were performed (Avermann et al., 2012), we set each maximal synaptic

454   conductance as the value needed to generate a PSP of the desired amplitude when the target

455   neuron started at resting potential in the case of EPSPs or -55mV in the case of IPSPs, which

456   we computed analytically. Refractory periods were calculated as the inter-spike-interval

457   corresponding to the maximal experimentally reported firing rate. Release probability and

458   synaptic strength values for unconnected neurons are excluded from Table 1. Excitatory

459   synaptic time constants were set at 2 ms, which is typical for the fast component of AMPA

460   receptor responses, but could not be estimated from the PSP statistics in Avermann et al.

461   (2012) because of masking by the slower membrane time constant. The mathematical form of

462   our model meant that inhibitory synaptic time constants needed to be equal for all incoming

463   inhibitory synapses to a neuron. We set these to 40 ms for E, $5HT_{3A}R$ and SOM neurons and

464   16 ms for PV neurons, which were the typical values of the IPSP decay time constants in the

465   Avermann et al. (2012) dataset. Due to lack of direct data for this circuit, connection

466   probabilities for synapses from L4 E neurons to E, PV and SOM L2/3 neurons was set to a

467   typical cortical value of 0.15, while $5HT_{3A}R$ neurons did not receive any input from L4 (Gentet

468   et al., 2012). Similarly due to a lack of direct data, we set synaptic release probabilities for

469   connections from L4 to L2/3 neurons to a typical cortical value of 0.25, while mean and median

470   L4 excitatory PSP amplitudes onto L2/3 PV and SOM were set to 0.8 and 0.48 mV,

471   respectively, to match reported data for L4 EPSP amplitudes onto L2/3 E neurons (Lefort et al.,

472   2009). L4 neuron dynamics were not explicitly simulated, but instead modeled only as a set of

473   output spike trains. After selecting the subset of active L4 neurons (see Results), spike times

474   were drawn randomly from a Gaussian distribution with standard deviation of 2 ms.

475   For the simulations presented in Figure 2 we varied only 76 model parameters, which is 24

476   less than the total number of 100 model parameters listed in Table 1. We excluded the four

477 neuronal refractory periods (because in almost all simulations each neuron spiked a maximum

478 of once, making the refractory period irrelevant), and the six connection probabilities that were

479 fixed at zero. Finally, we grouped together the mean and median PSP amplitudes for each of

480 the fourteen non-zero synaptic connections, so that both parameters were increased or

481 decreased by the same fraction in tandem. Together these choices reduced the number of test

482 parameters from 100 to 76.

483 For all parameters that naturally range from 0 upwards, such as the number of neurons or

484 release probability, we increased or decreased their values during testing in the most intuitive

485 way, by adding +/- 20% of the baseline value. However, this method was less useful for other

486 parameters, such as cell resting voltage, for which we reasoned it made more sense to scale

487 relative to another parameter, such as spike threshold. As a result, we varied 1) resting voltage

488 relative to its difference from spike threshold; 2) spike threshold relative to its difference with

489 resting voltage; 3) excitatory synaptic reversal potentials relative to resting voltage; 4) inhibitory

490 synaptic reversal potentials relative to spike threshold.

Table 1. L2/3 computational circuit model parameters and mean slope & threshold shifts.							
Parameter	Value	Source	+20% effect on slope, thresh	Parameter	Value	Source	+20% effect on slope, thresh
N_E	1700	[1]	slope: 6.4×10^{-3} thresh: 5.16	$pcon_{l5htE}$	0.465	[2]	slope: -3.25×10^{-3} thresh: -0.103
N_{lpv}	70	[1]	slope: 4.3×10^{-3} thresh: -1.51	$pcon_{l5htlpv}$	0.38	[2]	slope: -7.13×10^{-3} thresh: -0.298
N_{l5ht}	115	[1]	slope: -0.0104 thresh: -0.58	$pcon_{l5htl5ht}$	0.38	[2]	slope: 6.07×10^{-4} thresh: 0.175
N_{Isom}	45	[1]	slope: -0.001 thresh: -0.83	$pcon_{l5htIsom}$	0	No data	Not tested
N_{EL4}	1500	[1]	slope: -0.106 thresh: 3.43	$pcon_{IsomE}$	0.5	[5]	slope: -6.29×10^{-3} thresh: -0.8919
$Vrest_E$	-68 mV	[2]	slope: 0.049 thresh: -6.09	$pcon_{Isomlpv}$	0	No data	Not tested
$Vrest_{lpv}$	-68 mV	[2]	slope: -0.016 thresh: -0.963	$pcon_{Isoml5ht}$	0	No data	Not tested
$Vrest_{l5ht}$	-62 mV	[2]	slope: -9.48×10^{-4} thresh: 0.205	$pcon_{IsomIsom}$	0	No data	Not tested
$Vrest_{Isom}$	-57 mV	[3]	slope: 3.58×10^{-3} thresh: 0.034	$prel_{EL4E}$	0.25	No data	slope: -0.112 thresh: 4.21
Vth_E	-38 mV	[2]	slope: -3.76×10^{-3} thresh: -0.381	$prel_{EL4lpv}$	0.25	No data	slope: 0.0103 thresh: 0.682
Vth_{lpv}	-37.4 mV	[2]	slope: 3.87×10^{-3} thresh: 0.221	$prel_{EL4Isom}$	0.25	No data	slope: -2.06×10^{-3} thresh: -0.537
Vth_{l5ht}	-36 mV	[2]	slope: -1.12×10^{-3} thresh: 0.013	$prel_{EE}$	0.25	No data	slope: 4.99×10^{-3} thresh: 6.074
Vth_{Isom}	-40 mV	[3]	slope: -3.26×10^{-3} thresh: -0.083	$prel_{Elpv}$	0.25	No data	slope: -4.04×10^{-4} thresh: 0.163

Rin_E	160 MΩ	[2]	slope: 1.95 x10^{-3} thresh: -0.283	$prel_{EI5ht}$	0.25	No data	slope: -9.32 x10^{-3} thresh: -0.532
Rin_{Ipv}	100 MΩ	[2]	slope: -8.38 x10^{-3} thresh: -0.283	$prel_{EIsom}$	0.25	No data	slope: -7.32 x10^{-3} thresh: -0.3847
Rin_{I5ht}	200 MΩ	[2]	slope: -3.87 x10^{-3} thresh: -0.653	$prel_{IpvE}$	0.25	No data	slope: 1.03 x10^{-2} thresh: -0.941
Rin_{Isom}	250 MΩ	[4]	slope: 7.55 x10^{-3} thresh: 0.465	$prel_{IpvIpv}$	0.25	No data	slope: 1.21 x10^{-3} thresh: -0.061
τm_E	28 ms	[2]	slope: -9.59 x10^{-3} thresh: 0.268	$prel_{IpvI5ht}$	0.25	No data	slope: -4.73 x10^{-3} thresh: 0.011
τm_{Ipv}	21 ms	[2]	slope: 4.82 x10^{-3} thresh: 0.027	$prel_{I5htE}$	0.25	No data	slope: -1.63 x10^{-3} thresh: -0.379
τm_{I5ht}	10 ms	[2]	slope: -5.09 x10^{-3} thresh: -0.302	$prel_{I5htIpv}$	0.25	No data	slope: -3.41 x10^{-3} thresh: -0.262
τm_{Isom}	30 ms	[4]	slope: -2.89 x10^{-3} thresh: -0.159	$prel_{I5htI5ht}$	0.25	No data	slope: 3.05 x10^{-3} thresh: 0.123
$tref_E$	55.5 ms	[2]	Not tested	$p_{rel,IsomE}$	0.25	No data	slope: -2.13 x10^{-4} thresh: -0.65
$tref_{Ipv}$	5.4 ms	[2]	Not tested	$w_{EL4E,mean}$	0.8 mV	[1]	slope: -0.142 thresh: 0.342
$tref_{I5ht}$	21.3 ms	[2]	Not tested	$w_{EL4E,median}$	0.48 mV	[1]	slope: -0.142 thresh: 0.342
$tref_{Isom}$	20 ms	[3]	Not tested	$w_{EL4Ipv,mean}$	0.8 mV	$=w_{EL4E}$	slope: 3.61 x10^{-3} thresh: 6.54 x10^{-3}
$\tau syn_{E,e}$	2 ms	Typical	slope: 1.37 x10^{-2} thresh: -1.79	$w_{EL4Ipv,median}$	0.48 mV	$=w_{EL4E}$	slope: 3.61 x10^{-3} thresh: 6.54 x10^{-3}
$\tau syn_{E,i}$	40 ms	[2]	slope: -7.29 x10^{-3} thresh: 0.48	$w_{EL4Isom,mean}$	0.8 mV	$=w_{EL4E}$	slope: 5.05 x10^{-3} thresh: -0.329
$\tau syn_{Ipv,e}$	2 ms	Typical	slope: -9.79 x10^{-3} thresh: -0.477	$w_{EL4Isom,median}$	0.48 mV	$=w_{EL4E}$	slope: 5.05 x10^{-3} thresh: -0.329
$\tau syn_{Ipv,i}$	16 ms	[2]	slope: 1.56 x10^{-3} thresh: -0.097	$w_{EE,mean}$	0.37 mV	[2]	slope: 7.44 x10^{-3} thresh: 5.34
$\tau syn_{I5ht,e}$	2 ms	Typical	slope: 4.52 x10^{-3} thresh: -0.047	$w_{EE,median}$	0.2 mV	[2]	slope: 7.44 x10^{-3} thresh: 5.34
$\tau syn_{I5ht,i}$	40 ms	[2]	slope: -3.82 x10^{-3} thresh: -0.387	$w_{EIpv,mean}$	0.82 mV	[2]	slope: -3.77 x10^{-4} thresh: -0.297
$\tau syn_{Isom,e}$	2 ms	Typical	slope: -0.0126 thresh: -8.82 x10^{-3}	$w_{EIpv,median}$	0.68 mV	[2]	slope: -3.77 x10^{-4} thresh: -0.297
$\tau syn_{Isom,i}$	40 ms	[2]	slope: -4.88 x10^{-3} thresh: -0.301	$w_{EI5ht,mean}$	0.39 mV	[2]	slope: -6.81 x10^{-3} thresh: -0.46
$Erev_e$	0 mV	Typical	slope: -0.056 thresh: 1.53	$w_{EI5ht,median}$	0.19 mV	[2]	slope: -6.81 x10^{-3} thresh: -0.46
$Erev_{Ei}$	-68 mV	$=Vrest_E$	slope: 3.2x10^{-3} thresh: -3.77	$w_{EIsom,mean}$	0.5 mV	No data	slope: -3.61 x10^{-3} thresh: -0.359
$Erev_{Ipvi}$	-68 mV	$=Vrest_{Ipv}$	slope: -0.010 thresh: -0.617	$w_{EIsom,median}$	0.4 mV	No data	slope: -3.61 x10^{-3} thresh: -0.359
$Erev_{I5hti}$	-62 mV	$=Vrest_{I5ht}$	slope: 3.8x10^{-3} thresh: 0.132	$w_{IpvE,mean}$	0.52 mV	[2]	slope: 6.41 x10^{-3} thresh: -1.47
$Erev_{Isomi}$	-57 mV	$=Vrest_{Isom}$	slope: -4.2x10^{-3} thresh: -0.088	$w_{IpvE,median}$	-0.29 mV	[2]	slope: 6.41 x10^{-3} thresh: -1.47
$pcon_{EL4E}$	0.15	No data	slope: -0.121 thresh: 2.99	$w_{IpvIpv,mean}$	-0.56 mV	[2]	slope: -2.52 x10^{-3} thresh: -0.345
$pcon_{EL4Ipv}$	0.15	No data	slope: 1.38x10^{-3} thresh: 0.029	$w_{IpvIpv,median}$	-0.44 mV	[2]	slope: -2.52 x10^{-3} thresh: -0.345
$pcon_{EL4I5ht}$	0	No data	Not tested	$w_{IpvI5ht,mean}$	-0.83 mV	[2]	slope: -4.24 x10^{-3} thresh: -0.266
$pcon_{EL4Isom}$	0.15	No data	slope: 7.62 x10^{-3} thresh: -0.245	$w_{IpvI5ht,median}$	-0.6 mV	[2]	slope: -4.24 x10^{-3} thresh: -0.266

$pcon_{EE}$	0.17	[2]	slope: 5.86 x10^{-3} thresh: 6.084	$w_{I5htE,mean}$	-0.49 mV	[2]	slope: -3.61 x10^{-4} thresh: -0.018
$pcon_{EIpv}$	0.575	[2]	slope: -1.17 x10^{-3} thresh: -0.099	$w_{I5htE,median}$	-0.3 mV	[2]	slope: -3.61 x10^{-4} thresh: -0.018
$pcon_{EI5ht}$	0.24	[2]	slope: -6.44 x10^{-3} thresh: -0.541	$w_{I5htIpv,mean}$	-0.49 mV	[2]	slope: -1.77 x10^{-3} thresh: -0.187
$pcon_{EIsom}$	0.5	[5]	slope: -4.37 x10^{-3} thresh: -0.27	$w_{I5htIpv,median}$	-0.15 mV	[2]	slope: -1.77 x10^{-3} thresh: -0.187
$pcon_{IpvE}$	0.6	[2]	slope: 7.16 x10^{-3} thresh: -1.049	$w_{I5htI5ht,mean}$	-0.37 mV	[2]	slope: -4.12 x10^{-3} thresh: -0.416
$pcon_{IpvIpv}$	0.55	[2]	slope: -2.61 x10^{-3} thresh: -0.0456	$w_{I5htI5ht,median}$	-0.23 mV	[2]	slope: -4.12 x10^{-3} thresh: -0.416
$pcon_{IpvI5ht}$	0.24	[2]	slope: -2.81 x10^{-3} thresh: -0.458	$w_{IsomE,mean}$	-0.5 mV	No data	slope: -0.013 thresh: -0.984
$pcon_{IpvIsom}$	0	No data	Not tested	$w_{IsomE,median}$	-0.4 mV	No data	slope: -0.013 thresh: -0.984

Source [1] is Lefort et al. (2009), [2] is Avermann et al. (2012), [3] is Fanselow et al. (2008), [4] is Kinnischtzke et al. (2012), [5] is Fino and Yuste (2011). *N* is number of neurons, *Vrest* is resting potential, *Vth* is spike voltage threshold, *Rin* is input resistance, *tref* is refractory period, *τm* is the membrane time constant, *τsyn* is the synaptic time constant with the first subscript indicating the postsynaptic neuron type and the second subscript the neurotransmitter type of the presynaptic neuron (*e* or *i*), *Erev* is the synaptic reversal potential, *pcon* is the synaptic connection probability, *prel* is the synaptic release probability, *w* is the mean or median post-synaptic potential amplitude as indicated. For all neuronal parameters, the subscript indicates the neuron type: *E* is L2/3 excitatory neurons, *Ipv* is PV neurons, *I5ht* is 5HT$_{3A}$R neurons, *Isom* is SOM neurons, and *EL4* is L4 excitatory neurons. For synaptic parameters, the first and second subscripts indicate the pre- and post-synaptic neuron types, respectively.

Logistic model

From the L2/3 circuit model simulations, we numerically estimated the probability *q* that each neuron in the model fires a spike as a function of the fraction of L4 inputs that were active, *f*. We then used the generalized linear model regression tool in MATLAB to find the best fit of the two logistic model parameters for each neuron:

$$q(f) = \frac{1}{1 + \exp\left(-\beta\left(f - f_{1/2}\right)\right)} ,$$

where the parameter *β* represents the slope, and the parameter $f_{1/2}$ represents the fraction of active L4 neurons at which the response probability $q = 0.5$. For clarity of presentation, in the main text we converted this $f_{1/2}$ parameter to what we termed the 'threshold', f_{thresh}, which we defined as the fraction of L4 neurons needed to reach a specified spike probability, q_{thresh}.

512   Throughout the study we fixed $q_{thresh} = 0.01$. The threshold is related to $f_{1/2}$ via the inverse of

513   the logistic function

514    $f_{thresh} = f_{1/2} + \log\left(\frac{q_{thresh}}{1-q_{thresh}}\right)/\beta.$

515   We computed firing rates and pairwise correlations from the logistic model (Figures 3—4) in

516   the following way. First, we assumed that the fraction of active L4 neurons is described by a

517   normally distributed random variable with zero mean and unit variance:

518    $p(f) = \frac{\exp(-f^2/2)}{\sqrt{2\pi}} = \mathcal{N}(0,1)$.

519   We defined the β and $f_{1/2}$ parameters relative to the mean and standard deviation of the input

520   distribution. Since q is a monotonically increasing function of f, the probability distribution for q

521   is

$p(q) = p(f(q))\left|\frac{df}{dq}\right|$

522   where $f(q)$ is the inverse of the logistic function $q(f)$ and

523    $\frac{df}{dq} = \frac{\left(\exp\left(-\beta(f-f_{1/2})\right)+1\right)^2}{\beta \exp(-\beta(f-f_{1/2}))}$. We calculate a neuron's mean firing rate μ as the expectation of q,

524    $\mu = \mathbb{E}[q] = \int_0^1 [q \times p(q)]dq = \int_0^1 \left[q \times p(f(q))\left|\frac{df}{dq}\right|\right]dq.$

525   We calculate the pairwise covariance of two homogeneous neurons driven by a common input

526   f as

527    $\text{cov} = \mathbb{E}[q^2] - (\mathbb{E}[q])^2 = \mathbb{E}[q^2] - \mu^2 = \int_0^1 \left[q^2 \times p(f(q))\left|\frac{df}{dq}\right|\right]dq - \mu^2$, then find the pairwise

528   correlation by normalizing the covariance by the neurons' shared variance, $\text{var} = \mu(1-\mu)$.

529   For fitting the logistic model to the recorded neural firing rates and correlations (Figure 4), we

530   considered a population model where the joint probability distribution across threshold and

531   slope was specified by a 2D Gaussian, which has five parameters: threshold mean and s.d.,

532   slope mean and s.d., and slope-threshold correlation. The three constraint statistics we

533   considered from the neural population data were the mean neural ON probability, the s.d. of

534   neural ON probabilities, and the mean pairwise correlations. We found the best-fit model

535   parameters for each dataset using stochastic gradient descent. We checked for fit

536   convergence by sampling a large number of logistic model parameters from the fitted 2D

537   Gaussian, drawing binary samples from these logistic 'neurons' and computing the ON

538   probability mean and s.d., and mean pairwise correlation from the synthetic binary samples,

539   and comparing the computed statistical values to the original data statistics. For the sensitivity

540   analysis presented in Figure 5, we numerically computed the partial derivative in mean firing

541   rate and pairwise correlation with respect to the mean slope and mean threshold parameters in

542   the population logistical model, using standard finite difference methods.

543   ***Statistical tests***

544   To avoid parametric assumptions, all statistical tests were done using standard bootstrapping

545   methods with custom-written MATLAB scripts. For example when assessing the observed

546   difference between two group means $\Delta\mu_{obs}$ we performed the following procedure to calculate

547   a p-value. First we pool the data points from the two groups to create a null set S_{null}. We then

548   construct two hypothetical groups of samples S_1 and S_2 from this by randomly drawing n_1 and

549   n_2 samples with replacement from S_{null}, where n_1 and n_2 are the number of data points in the

550   original groups 1 and 2 respectively. We take the mean of both hypothetical sets $\Delta\mu_1$ and $\Delta\mu_2$

551   and calculate their difference $\Delta\mu_{null} = \Delta\mu_1 - \Delta\mu_2$. We then repeat the entire procedure 10^7

552   times to build up a histogram of $\Delta\mu_{null}$. This distribution is always centered at zero. After

553   normalizing, this can be interpreted as the probability distribution $f(\Delta\mu_{null})$ for observing a group

554   mean difference of $\Delta\mu_{null}$ purely by chance if the data were actually sampled from the same

555   null distribution. Then the final p-value for the probability of finding a group difference of at

556   least $\Delta\mu_{obs}$ in either direction is given by $p = \int_{-\infty}^{-\Delta\mu_{obs}} f(\Delta\mu_{null})d\Delta\mu_{null} + \int_{\Delta\mu_{obs}}^{\infty} f(\Delta\mu_{null})d\Delta\mu_{null}$.

557   ***Conversion from firing rate to ON/OFF probabilities for Ca^{2+} imaging data***

558   For the Ca^{2+} imaging data, we began with estimated firing rate time series $r_i(t)$ for each neuron

559   i recorded as part of a population of N neurons. For later parts of the analysis we needed to

560   convert these firing rates to binary ON/OFF values. This conversion involves a choice. One

561   option would be to simply threshold the data, but this would throw away information about the

562   magnitude of the firing rate. We instead take a probabilistic approach where rather than

563   deciding definitively whether a given neuron was ON or OFF in a given time bin, we calculate

564   the probability that the neuron was ON or OFF by assuming that neurons fire action potentials

28

565   according to an inhomogeneous Poisson process with rate r_i(t). The mean number of spikes

566    $\lambda_i(t)$ expected in a time bin of width Δt is $\lambda_i(t) = r_i(t)\Delta t$. We choose $\Delta t = 1$ second. Under the

567   Poisson model the actual number of spikes m in a particular time bin is a random variable that

568   follows the Poisson distribution $P(m=k) = \lambda^k \exp(-\lambda) / k!$. We considered a neuron active (ON) if

569   it is firing one or more spikes in a given time bin. Hence the probability that a neuron is ON is

570    $p_{on}(t)=1-P(m=0)=1-\exp(\lambda)$. This approach has two advantages over thresholding: 1) it

571   preserves some information about the magnitude of firing rates, and 2) it acts to regularize the

572   probability distribution for the number of neurons active by essentially smoothing nearby values

573   together.

574   ***Entropy estimation for large numbers of neurons***

575   Entropy was estimated by fitting a statistical model we recently developed, called the

576   population tracking model (O'Donnell et al., in press), to the binarized Ca^{2+} imaging data.

577   Briefly, the population tracking model fits two aspects of the data: the probability distribution for

578   the number of neurons synchronously active in the population, and also the conditional firing

579   probability that each individual neuron is active given the population count. Hence the model

580   captures both some aggregate statistics of the population activity, and some aspects of the

581   heterogeneity across neurons. See O'Donnell et al., (in press) for complete details and

582   validation of the method. Code for fitting the model to data is available at

583   https://github.com/cianodonnell/PopulationTracking.

584   The entropy/neuron generally decreased with the number of neurons considered as result of

585   the population correlations (Figure 6B), so we needed to control for neural population size

586   when comparing data from different experimental groups. On the one hand, we would like to

587   study as large a number of neurons as possible, because we expect the effects of collective

588   network dynamics to be stronger for large population sizes and this may be the regime where

589   differences between the groups emerge. On the other hand, our recording methods allowed us

590   to sample only typically around ~100 neurons at a time, and as few as 40 neurons in some

591   animals. Hence we proceeded by first estimating the entropy/neuron in each animal by

592   calculating the entropy of random subsets of neurons of varying size from 10 to 100 (if

593   possible) in steps of 10. For each population size we sampled a large number of independent

594   subsets, calculated the entropy of each. Finally, for each dataset we fit a double exponential

595   function to the estimated entropy/neuron as a function of the number of neurons: $H/N = A*\exp(-b*N) + C*\exp(-d*N) + e$, and used this fit to estimate H/N for 100 neurons.

596

597

598   **Acknowledgements**
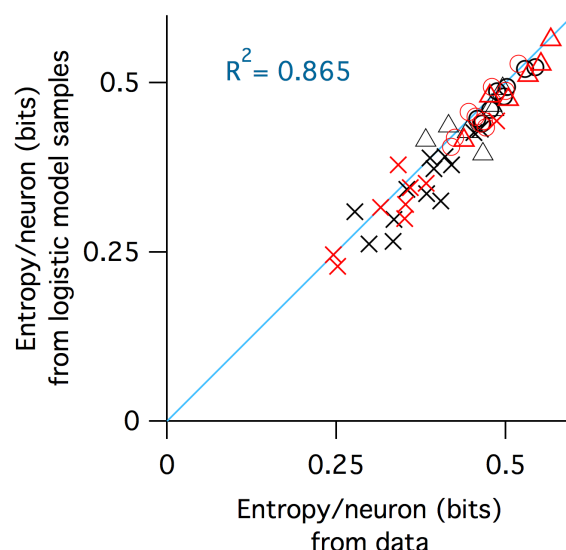
Supp Fig 1. Agreement between entropy estimated from raw data and entropy estimated from samples from fitted logistic models. Black symbols are WT, red are KO. Crosses are P9—11, circles P14—16, triangles P30—40. Blue line is identity, the R^2 value of which is reported in the inset.

References

Avermann, M., Tomm, C., Mateo, C., Gerstner, W., Petersen, C.C.H., 2012. Microcircuits of excitatory and inhibitory neurons in layer 2/3 of mouse barrel cortex. J Neurophysiol 107, 3116–3134. doi:10.1152/jn.00917.2011

Bateup, H.S., Takasaki, K.T., Saulnier, J.L., Denefrio, C.L., Sabatini, B.L., 2011. Loss of Tsc1 in vivo impairs hippocampal mGluR-LTD and increases excitatory synaptic function. J Neurosci 31, 8862–8869. doi:10.1523/JNEUROSCI.1617-11.2011

Berkes, P., Orbán, G., Lengyel, M., Fiser, J., 2011. Spontaneous cortical activity reveals hallmarks of an optimal internal model of the environment. Science 331, 83–87. doi:10.1126/science.1195870

Berzhanskaya, J., Phillips, M.A., Shen, J., Colonnese, M.T., 2016. Sensory hypo-excitability in a rat model of fetal development in Fragile X Syndrome. Sci Rep 6, 30769. doi:10.1038/srep30769

Braat, S., Kooy, R.F., 2015. The GABAA Receptor as a Therapeutic Target for Neurodevelopmental Disorders. Neuron 86, 1119–1130. doi:10.1016/j.neuron.2015.03.042

Bureau, I., Shepherd, G.M.G., Svoboda, K., 2008. Circuit and plasticity defects in the developing somatosensory cortex of FMR1 knock-out mice. J Neurosci 28, 5178–5188. doi:10.1523/JNEUROSCI.1076-08.2008

Clancy, K.B., Schnepel, P., Rao, A.T., Feldman, D.E., 2015. Structure of a single whisker representation in layer 2 of mouse somatosensory cortex. J Neurosci 35, 3946–3958. doi:10.1523/JNEUROSCI.3887-14.2015

Contractor, A., Klyachko, V.A., Portera-Cailliau, C., 2015. Altered Neuronal and Circuit Excitability in Fragile X Syndrome. Neuron 87, 699–715. doi:10.1016/j.neuron.2015.06.017

Cover, T.M., Thomas, J.A., 2006. Elements of Information Theory, 2nd ed. Wiley-Interscience.

Cruz-Martin, A., Crespo, M., Portera-Cailliau, C., 2010. Delayed Stabilization of Dendritic Spines in Fragile X Mice. J Neurosci 30, 7793–7803. doi:10.1523/JNEUROSCI.0577-10.2010

Dani, V.S., Chang, Q., Maffei, A., Turrigiano, G.G., Jaenisch, R., Nelson, S.B., 2005. Reduced cortical activity due to a shift in the balance between excitation and inhibition in a mouse model of Rett syndrome. Proc. Natl. Acad. Sci. U.S.A. 102, 12560–12565. doi:10.1073/pnas.0506071102

Fanselow, E.E., Richardson, K.A., Connors, B.W., 2008. Selective, state-dependent activation of somatostatin-expressing inhibitory interneurons in mouse neocortex. J Neurophysiol 100, 2640–2652. doi:10.1152/jn.90691.2008

Fino, E., Yuste, R., 2011. Dense inhibitory connectivity in neocortex. Neuron 69, 1188–1203. doi:10.1016/j.neuron.2011.02.025

Gentet, L.J., Kremer, Y., Taniguchi, H., Huang, Z.J., Staiger, J.F., Petersen, C.C.H., 2012. Unique functional properties of somatostatin-expressing GABAergic neurons in mouse barrel cortex. Nat Neurosci 15, 607–612. doi:10.1038/nn.3051

Gibson, J.R., Bartley, A.F., Hays, S.A., Huber, K.M., 2008. Imbalance of neocortical excitation and inhibition and altered UP states reflect network hyperexcitability in the mouse model of fragile X syndrome. J Neurophysiol 100, 2615–2626. doi:10.1152/jn.90752.2008

Golshani, P., Gonçalves, J.T., Khoshkhoo, S., Mostany, R., Smirnakis, S., Portera-Cailliau, C.,

646   2009. Internally mediated developmental desynchronization of neocortical network activity.
647   J Neurosci 29, 10890–10899. doi:10.1523/JNEUROSCI.2012-09.2009
648 Gonçalves, J.T., Anstey, J.E., Golshani, P., Portera-Cailliau, C., 2013. Circuit level defects in
649   the developing neocortex of Fragile X mice. Nat Neurosci 16, 903–909.
650   doi:10.1038/nn.3415
651 Goodman, D.F.M., Brette, R., 2009. The brian simulator. Front Neurosci 3, 192–197.
652   doi:10.3389/neuro.01.026.2009
653 Gutenkunst, R.N., Waterfall, J.J., Casey, F.P., Brown, K.S., Myers, C.R., Sethna, J.P., 2007.
654   Universally sloppy parameter sensitivities in systems biology models. PLoS Comput Biol 3,
655   1871–1878. doi:10.1371/journal.pcbi.0030189
656 Harlow, E.G., Till, S.M., Russell, T.A., Wijetunge, L.S., Kind, P., Contractor, A., 2010. Critical
657   period plasticity is disrupted in the barrel cortex of FMR1 knockout mice. Neuron 65, 385–
658   398. doi:10.1016/j.neuron.2010.01.024
659 Hays, S.A., Huber, K.M., Gibson, J.R., 2011. Altered neocortical rhythmic activity states in
660   Fmr1 KO mice are due to enhanced mGluR5 signaling and involve changes in excitatory
661   circuitry. J Neurosci 31, 14223–14234. doi:10.1523/JNEUROSCI.3157-11.2011
662 He, Q., Nomura, T., Xu, J., Contractor, A., 2014. The developmental switch in GABA polarity is
663   delayed in fragile X mice. J Neurosci 34, 446–450. doi:10.1523/JNEUROSCI.4447-13.2014
664 Kehrer, C., Maziashvili, N., Dugladze, T., Gloveli, T., 2008. Altered Excitatory-Inhibitory
665   Balance in the NMDA-Hypofunction Model of Schizophrenia. Frontiers in Molecular
666   Neuroscience 1, 6. doi:10.3389/neuro.02.006.2008
667 Kerr, J.N.D., de Kock, C.P.J., Greenberg, D.S., Bruno, R.M., Sakmann, B., Helmchen, F., 2007.
668   Spatial organization of neuronal population responses in layer 2/3 of rat barrel cortex. J
669   Neurosci 27, 13316–13328. doi:10.1523/JNEUROSCI.2210-07.2007
670 Kinnischtzke, A.K., Sewall, A.M., Berkepile, J.M., Fanselow, E.E., 2012. Postnatal maturation
671   of somatostatin-expressing inhibitory cells in the somatosensory cortex of GIN mice. Front
672   Neural Circuits 6, 33. doi:10.3389/fncir.2012.00033
673 La Fata, G., Gärtner, A., Domínguez-Iturza, N., Dresselaers, T., Dawitz, J., Poorthuis, R.B.,
674   Averna, M., Himmelreich, U., Meredith, R.M., Achsel, T., Dotti, C.G., Bagni, C., 2014.
675   FMRP regulates multipolar to bipolar transition affecting neuronal migration and cortical
676   circuitry. Nat Neurosci. doi:10.1038/nn.3870
677 Lefort, S., Tomm, C., Floyd Sarria, J.-C., Petersen, C.C.H., 2009. The excitatory neuronal
678   network of the C2 barrel column in mouse primary somatosensory cortex. Neuron 61, 301–
679   316. doi:10.1016/j.neuron.2008.12.020
680 Lu, H., Ash, R.T., He, L., Kee, S.E., Wang, W., Yu, D., Hao, S., Meng, X., Ure, K., Ito-Ishida, A.,
681   Tang, B., Sun, Y., Ji, D., Tang, J., Arenkiel, B.R., Smirnakis, S.M., Zoghbi, H.Y., 2016.
682   Loss and Gain of MeCP2 Cause Similar Hippocampal Circuit Dysfunction that Is Rescued
683   by Deep Brain Stimulation in a Rett Syndrome Mouse Model. Neuron 91, 739–747.
684   doi:10.1016/j.neuron.2016.07.018
685 Luczak, A., Bartho, P., Harris, K.D., 2009. Spontaneous events outline the realm of possible
686   sensory responses in neocortical populations. Neuron 62, 413–425.
687   doi:10.1016/j.neuron.2009.03.014
688 Mao, T., Kusefoglu, D., Hooks, B.M., Huber, D., Petreanu, L., Svoboda, K., 2011. Long-range
689   neuronal circuits underlying the interaction between sensory and motor cortex. Neuron 72,

690   111–123. doi:10.1016/j.neuron.2011.07.029

691 Meredith, R.M., Dawitz, J., Kramvis, I., 2012. Sensitive time-windows for susceptibility in
692   neurodevelopmental disorders. Trends Neurosci 35, 335–344.
693   doi:10.1016/j.tins.2012.03.005

694 Miller, J.-E.K., Ayzenshtat, I., Carrillo-Reid, L., Yuste, R., 2014. Visual stimuli recruit
695   intrinsically generated cortical ensembles. 111, E4053–E4061.
696   doi:10.1073/pnas.1406077111

697 Mitra, A., Snyder, A.Z., Blazey, T., Raichle, M.E., 2015. Lag threads organize the brain's
698   intrinsic activity. Proc. Natl. Acad. Sci. U.S.A. 112, E2235–E2244.
699   doi:10.1073/pnas.1503960112

700 O'Leary, T., Sutton, A.C., Marder, E., 2015. Computational models in the age of large datasets.
701   Curr Opin Neurobiol 32C, 87–94. doi:10.1016/j.conb.2015.01.006

702 Paluszkiewicz, S.M., Olmos-Serrano, J.L., Corbin, J.G., Huntsman, M.M., 2011. Impaired
703   inhibitory control of cortical synchronization in fragile X syndrome. J Neurophysiol 106,
704   2264–2272. doi:10.1152/jn.00421.2011

705 Patel, A.B., Hays, S.A., Bureau, I., Huber, K.M., Gibson, J.R., 2013. A target cell-specific role
706   for presynaptic Fmr1 in regulating glutamate release onto neocortical fast-spiking inhibitory
707   neurons. J Neurosci 33, 2593–2604. doi:10.1523/JNEUROSCI.2447-12.2013

708 Petersen, C.C.H., Crochet, S., 2013. Synaptic computation and sensory processing in
709   neocortical layer 2/3. Neuron 78, 28–48. doi:10.1016/j.neuron.2013.03.020

710 Petreanu, L., Huber, D., Sobczyk, A., Svoboda, K., 2007. Channelrhodopsin-2-assisted circuit
711   mapping of long-range callosal projections., Nature neuroscience. doi:10.1038/nn1891

712 Pologruto, T.A., Yasuda, R., Svoboda, K., 2004. Monitoring neural activity and [Ca2+] with
713   genetically encoded Ca2+ indicators. J Neurosci 24, 9572–9579.
714   doi:10.1523/JNEUROSCI.2854-04.2004

715 Qian, N., Lipkin, R.M., 2011. A learning-style theory for understanding autistic behaviors. Front
716   Hum Neurosci 5, 77. doi:10.3389/fnhum.2011.00077

717 Quian Quiroga, R., Panzeri, S., 2009. Extracting information from neuronal populations:
718   information theory and decoding approaches. Nat Rev Neurosci 10, 173–185.
719   doi:10.1038/nrn2578

720 Ringach, D.L., 2009. Spontaneous and driven cortical activity: implications for computation.
721   Curr Opin Neurobiol 19, 439–444. doi:10.1016/j.conb.2009.07.005

722 Rochefort, N.L., Garaschuk, O., Milos, R.-I., Narushima, M., Marandi, N., Pichler, B.,
723   Kovalchuk, Y., Konnerth, A., 2009. Sparsification of neuronal activity in the visual cortex at
724   eye-opening. 106, 15049–15054. doi:10.1073/pnas.0907660106

725 Rubenstein, J.L.R., Merzenich, M.M., 2003. Model of autism: increased ratio of
726   excitation/inhibition in key neural systems. Genes Brain Behav. 2, 255–267.

727 Sato, T.R., Gray, N.W., Mainen, Z.F., Svoboda, K., 2007. The functional microarchitecture of
728   the mouse barrel cortex. PLoS Biol 5, e189. doi:10.1371/journal.pbio.0050189

729 Schneidman, E., Berry, M.J., Segev, R., Bialek, W., 2006. Weak pairwise correlations imply
730   strongly correlated network states in a neural population. Nature 440, 1007–1012.
731   doi:10.1038/nature04701

732 Selby, L., Zhang, C., Sun, Q.-Q., 2007. Major defects in neocortical GABAergic inhibitory
733   circuits in mice lacking the fragile X mental retardation protein. Neurosci. Lett. 412, 227–

734   232. doi:10.1016/j.neulet.2006.11.062

735 Testa-Silva, G., Loebel, A., Giugliano, M., de Kock, C.P.J., Mansvelder, H.D., Meredith, R.M.,
736   2012. Hyperconnectivity and slow synapses during early development of medial prefrontal
737   cortex in a mouse model for mental retardation and autism. Cereb Cortex 22, 1333–1342.
738   doi:10.1093/cercor/bhr224

739 Tomm, C., Avermann, M., Petersen, C., Gerstner, W., Vogels, T.P., 2014. Connection-type-
740   specific biases make uniform random network models consistent with cortical recordings. J
741   Neurophysiol 112, 1801–1814. doi:10.1152/jn.00629.2013

742 Wallace, M.L., Burette, A.C., Weinberg, R.J., Philpot, B.D., 2012. Maternal loss of Ube3a
743   produces an excitatory/inhibitory imbalance through neuron type-specific synaptic defects.
744   Neuron 74, 793–800. doi:10.1016/j.neuron.2012.03.036

745 Yaksi, E., Friedrich, R.W., 2006. Reconstruction of firing rate changes across neuronal
746   populations by temporally deconvolved Ca2+ imaging. Nat. Methods 3, 377–383.
747   doi:10.1038/nmeth874

748